Soft Matter

Elongation and percolation of defect motifs in anisotropic packing problems

Journal:	*Soft Matter*
Manuscript ID	SM-ART-12-2020-002174.R2
Article Type:	Paper
Date Submitted by the Author:	01-Apr-2021
Complete List of Authors:	Xie, Zhaoyu; Tufts University School of Arts and Sciences, Physics and Astronomy Atherton, Tim; Tufts University, Physics and Astronomy

Journal Name

ARTICLE TYPE

Cite this: DOI: 00.0000/xxxxxxxxxx

Elongation and percolation of defect motifs in anisotropic packing problems

Zhaoyu Xie,[a] and Timothy J. Atherton*[a]

Received Date
Accepted Date

DOI: 00.0000/xxxxxxxxxx

We examine the regime between crystalline and amorphous packings of anisotropic objects on surfaces of different genus by continuously varying their size distribution or shape from monodispersed spheres to bidispersed mixtures or monodispersed ellipsoidal particles; we also consider an anisotropic variant of the Thomson problem with a mixture of charges. With increasing anisotropy, we first observe the disruption of translational order with an intermediate orientationally ordered hexatic phase as proposed by Nelson, Rubinstein and Spaepen, and then a transition to amorphous state. By analyzing the structure of the disclination motifs induced, we show that the hexatic-amorphous transition is caused by the growth and connection of disclination grain boundaries, suggesting this transition lies in the percolation universality class in the scenarios considered.

1 Introduction

Packing problems, where a set of objects are arranged in a specified container to optimize the density, are an important model of many materials including granular media, colloids and amorphous solids[1–6]. In two-dimensional unbounded Euclidean space, the highest-density packing of disks is the hexagonal lattice where each particle is surrounded by six neighbors. Numerous situations where this highly regular crystalline arrangement becomes disordered have been explored: If the boundaries of the container are not commensurate with the lattice[7,8], or if the packing occurs on a curved surface so that the lattice is incompatible with the curvature[9–12], or if the particles are no longer circular and equal in size[13–16], the overall arrangement may lose either translational or orientational order, or both.

Topological defects, deviations from crystalline order that cannot be removed by continuous deformations, are an invaluable concept to understand the resulting packings. The elementary defect in a hexagonal lattice is a *disclination*, a site that possesses a coordination number $n \neq 6$; these tend to disrupt the orientational order as they promote rotation of the lattice vectors. Interactions between disclinations are analogous to electrostatics, motivating the definition of a topological charge $q = (6-n)$. Other defect motifs that occur include *dislocations*, disclination dipoles, *scars*, chains of disclinations of alternating sign that are induced on curved surfaces to accommodate the curvature[10], *pleats* that are bound to the edge of an open curved manifold[11] and *grain boundaries* that separate uncorrelated regions of crystalline order[17].

Consider perturbing the crystalline packing of monodispersed disks of radius r by replacing some fraction χ with a larger radius R such that $R/r > 1$. We may define a dimensionless parameter, the bidispersity $b = (R-r)/(R+r) \in [0,1]$, to describe the deviation from monodispersity. As b increases, Nelson, Rubinstein and Spaepen (NRS)[7,8] predict the following sequence: first dislocations appear introducing stacking faults that disrupt long range translational order. There then exists an intermediate *hexatic* phase that possesses either long range or power-law orientational order as the lattice vectors of adjacent patches of crystal remain correlated. Further increasing b leads to an amorphous phase that lacks both translational and orientational order. The hexatic phase is a zero-temperature analog of the intermediate hexatic phase that mediates melting in the Kosterlitz-Thouless-Halperin-Nelson-Young theory[18–20]. This phase transition into the amorphous phase triggered by the unbinding of topological defects also occurs in systems of hard disks[21,22], hard regular polygons[23], soft disks with repulsive power-law interactions[24,25] and active Brownian particles[26,27].

On a curved surface, such as a sphere, the NRS picture must be modified because defects are required even in the ground state, leading to a regime referred to as *spherical crystallography*[1,9,10], and vector transport properties of the curved surface complicates the measurement of long-range orientational correlations[28–30]. Isolated disclinations occur for a small number of particles N while for large N these become spatially extended *scars* trading off the free energy cost of creating additional defects in order to reduce deformation of the lattice[9,10]. On spheres, these structures are icosahedrally ordered[29], while the distribution for less

[a]Department of Physics and Astronomy, Tufts University, 574 Boston Avenue, Medford, Massachusetts 02155, USA. E-mail: timothy.atherton@tufts.edu

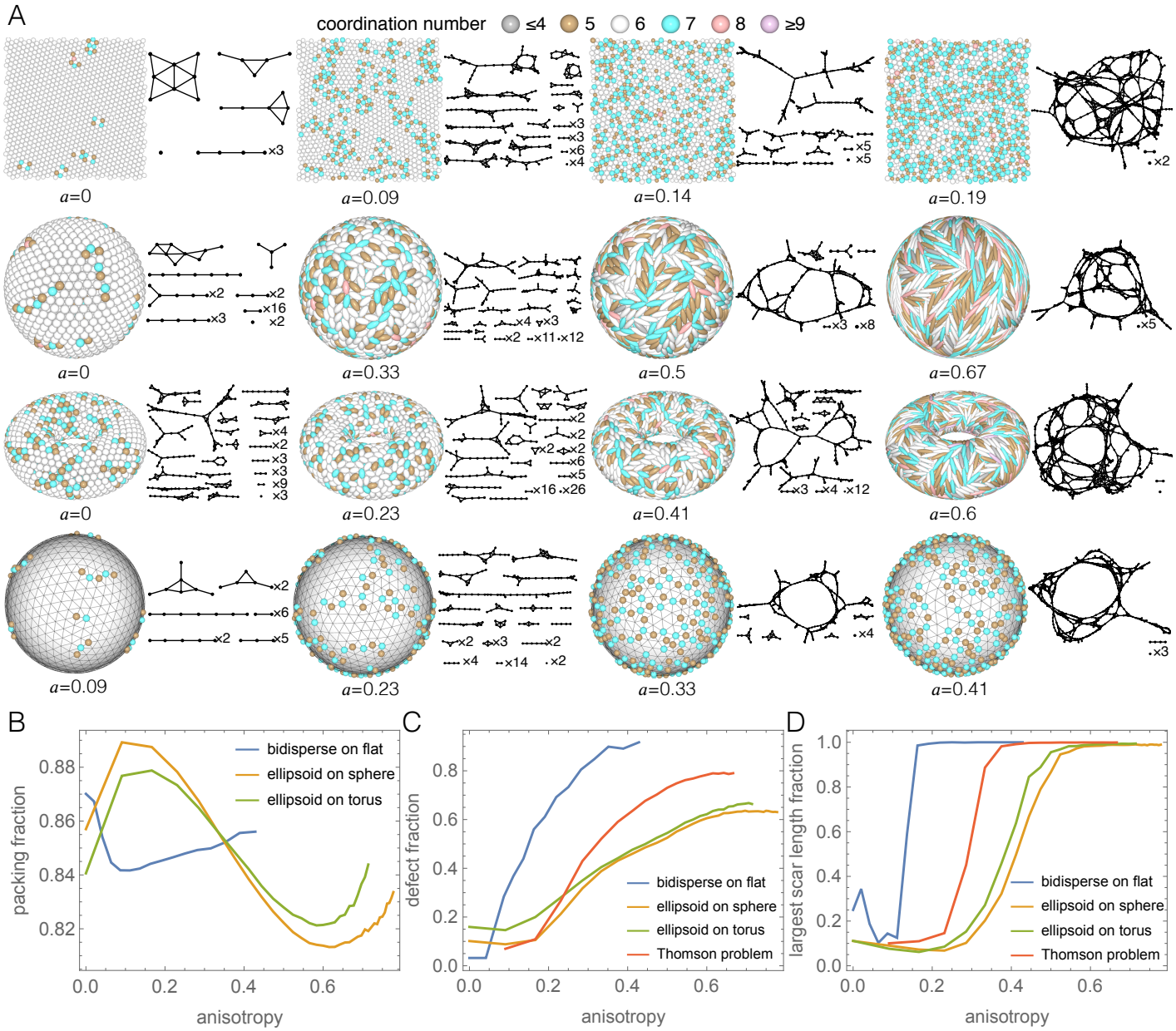

Fig. 1 Elongation and percolation of defect networks occurs with increasing anisotropy in a variety of anisotropic packing problems. (A) Packings as a function of anisotropy with particles colored by coordination number; the defect subgraph for each packing is calculated from the neighbor graph by retaining only non-hexagonally coordinated vertices. (B) Packing fraction as a function of anisotropy. (C) Fraction of defects and (D) the fraction of largest scar length as a function of anisotropy show a characteristic shape that is a signature of the percolation transition.

symmetric surfaces is driven by the distribution of Gaussian curvature [1,10,11,31–34].

We recently showed for packing bidispersed spheres on a sphere that as the bidispersity is increased from zero, the defect motifs begin to elongate above a critical value of bidispersity $b = 0.08$, continue to grow and eventually form a connected structure; at the same time the orientational order parameter becomes increasingly short range [35]. The hexatic-amorphous transition in this specific system may therefore be equivalently viewed as elongation and percolation of the scars, providing a connection between the regimes of spherical crystallography and random close packing and, by leveraging the results of percolation theory [36,37], successfully predicting the distribution and microstructure of the defects.

An obvious question arises whether the percolation of defects also applies to the NRS picture since the behaviors of defects are rather similar as the system goes to amorphous phase. Additionally, it is natural to ask whether the percolation mechanism is universal for other amorphization scenarios on surfaces of different geometry. Understanding the organization of defects can help design particle structures for multiple applications, such as colloidosomes [38], photonic crystals [39] or building blocks for new materials [40]. Particle anisotropy has also been shown to play a key role in local unjamming in biological media [41].

In this work, we demonstrate that the percolation mechanism occurs in the original NRS scenario, and for many other kinds of anisotropy that could be present. We examine: bidispersed mixtures on flat surfaces as considered by NRS, mixtures of identical elongated particles of varying aspect ratio λ, such as ellipsoids, on curved surfaces of different topology. We also consider a system with long-range interactions, an anisotropic generalization of the Thomson problem [42–44], whereby mixtures of different charge with ratio $\rho = q_2/q_1$ are arranged to minimize the electrostatic energy. Henceforth, we shall unify all these measures of anisotropy by collectively defining a single parameter $a \in [0,1]$, which depending on the system may be the bidispersity $(R-r)/(R+r)$, shape anisotropy $(\lambda-1)/(\lambda+1)$ or charge anisotropy $(q_2-q_1)/(q_1+q_2)$.

2 Results & Discussion

To do so, we generate packings of $N = 1000$ particles on flat surfaces, spherical surfaces and toroidal surfaces with aspect ratio 2, using a Monte Carlo procedure inspired by the Lubachevsky-Stillinger algorithm [45,46]: particles are initially randomly placed on a large surface, then diffuse both translationally and rotationally by Brownian motion while the size of the suface is gradually reduced. After reduction moves, gradient descent is performed on an objective function that penalizes overlaps. If overlaps cannot be removed, the algorithm backtracks and reduces the rate of reduction; the algorithm is halted when the reduction rate reaches a critical threshold. For bidispersed packings, a fraction $\chi = \frac{1}{2}$ of particles are inflated. Details of this algorithm are presented in previous work [35,47,48] and necessary modifications to deal with anisotropic particles are described in Methods below. For the Thomson problem, all charges are initially set equal and a minimum is found by conjugate gradient descent; a fraction $\chi = \frac{1}{2}$ of charges are randomly selected and increased in magnitude; then the energy is reminimized.

Disclinations are identified by the following procedure: We first generate a Voronoi diagram that approximates the navigation map [49,50] from a cloud of points generated to lie on the boundary of the particles; particles that possess a connected edge in this graph are identified as neighbors. From the resulting neighbor graph, we find the *subgraph* of defects, i.e. vertices that have connectivity other than 6.

Representative packings as a function of anisotropy a and their corresponding defect subgraphs are shown in Fig. 1A. Note that the representation of the subgraphs displayed here is designed to emphasize the topological features; there is no significance to the spatial position of the nodes. For monodispersed particles, the packings are crystalline as expected. On the flat surface, a few isolated defect motifs are typically present because the lattice may be incommensurate with the periodic boundary conditions. On curved surfaces the scars of spherical crystallography occur together with a number of dislocations. While defects are not topologically required on the torus, because the genus is 1 and the Euler characteristic is 0, the higher curvature present locally deforms the crystal lattice and therefore tends to promote longer scars and star motifs. As the degree of anisotropy is increased, the size of the defect motifs increases for all cases, and, eventually, a system-spanning structure emerges. In these packings, our focus is the process of elongation of defect networks hence packings beyond the system-spanning structures are not the interest of this manuscript.

The packing fraction as a function of anisotropy a for bidispersed spheres on the flat surface and ellipsoids on the surface of a sphere or a torus are displayed in Fig. 1B. For the bidispersed mixture, as a increases, the packing fraction decreases initially due to the introduction of disorder and afterwards slowly increases because the small particles tend to fill in the gap between large particles, consistent with the research on spherical surface [35]. On the contrary, for ellipsoids, when a increases, the packing fraction also increases to balance the additional rotational degree of freedom then decreases due to exclusion-volume effects, in agreement with previous results [14].

In Fig. 1C we show how the fraction of defects p varies as a function of the relevant anisotropy parameter a, showing that although the detailed variation of p depends on the particular scenario considered, these have a similar functional form: As, $a \to 0$, p is small and constant. Above a certain value of a, p begins to increase rapidly and eventually saturates. The value of anisotropy at which defect clusters begin to form, and the ultimate value of p, varies between the scenarios considered; ellipsoidal packings saturate at a significantly lower p than for the isotropically shaped particles; increasing the charge ratios in Thomson problem can achieve a larger p than elongated particles.

In Fig. 1D, we also display the growth of a spanning structure indicated by the fraction of scar length of the largest connected defect subgraph among all defects for various extent of anisotropy a in different systems. The fraction quickly rises to 1 as we increase the anisotropy, indicating the percolation transition occurs with the formation of a globally connected cluster. Also note that

the formation of a system-spanning structure is slower by varying the shape of particles than by adding bidispersity. We note that a rescaling of the form $a \to a^{\alpha}$ can be used to bring the transition points of the different scenarios into alignment and hence partially collapse the curves in both Fig. 1C and D. The physical significance of these powers remains unclear, however, and hence understanding the detailed form of these curves is left to future work.

As the degree of anisotropy and defect motifs increase in size, the system goes from crystalline phase into the amorphous phase as indicated by various structural order parameters. The translational order can be examined by the pair correlation function[28,30,51,52] $g(r) = \rho(r)/\rho_0$ where ρ_0 is the overall density of particles and $\rho(r)$ is the density at distance r from the centered reference particle. The local orientational order of particle i can be measured by bond orientational order $\psi_6(\vec{r_i}) = \sum \exp(i6\theta_{ij})/n$, where θ_{ij} is the angle of the bond connecting particle i and its neighbor j with respect to some local axis and n is the number of nearest neighbors. The bond orientational correlation function

$$G_6(r = |\vec{r_i} - \vec{r_j}|) = \langle \psi_6^*(\vec{r_i})\psi_6(\vec{r_j})\rangle,$$

displays the global orientational order[7,8,22,29,53–56]. Previous work[29] points out that vector transport on the curved surface complicates measurement of this quantity in contrast to flat space where a global reference coordinate system can be defined, and develops a procedure of selecting proper local reference axis to calculate ψ_6 on spherical surfaces, where the particles are projected onto the faces of the icosahedron whose vertices are aligned with the position of defects and then the local reference axis on each face is determined such that they are in the same direction after the icosahedron is unfolded onto a plane; further details are presented in Methods below. We use the angle θ to represent the distance between two particles on spherical surfaces.

Fig. 2 displays the evolution of g and G_6 with increasing anisotropy for bidispersed packings on flat surfaces and ellipsoidal particles on spherical surfaces. On flat surfaces(Fig. 2A&B), we recover the NRS results: the system is in crystalline phase at $b = 0$, with both translational order and orientational order over the whole system. As b goes above 0.04, the translational order becomes short range but the orientational order remains from the algebraical decay of G_6, indicating the packing is in the hexatic phase. After that, exponential decay of G_6 marks the system entering amorphous phase. For ellipsoidal packings on spherical surface(Fig. 2C&D), initially the system has long range order without anisotropy. As the particles are elongated, the long range order is lost with G_6 turning into algebraical and then exponential decay as the system transitions into the hexatic phase and then the amorphous phase.

We now show that this transition lies in the percolation universality class, which describes systems with a parameter p that controls the occupancy of sites or bonds. With increasing p, clusters of connected components arise with increasing size, and above a critical value p_c, the mean cluster size diverges for infinite lattices. The value of p_c depends on details of the particular system, but in the vicinity of $p \to p_c$, the cluster size distribution and structure exhibit universal behavior: For example, the clusters become fractalline and the cluster radius R,

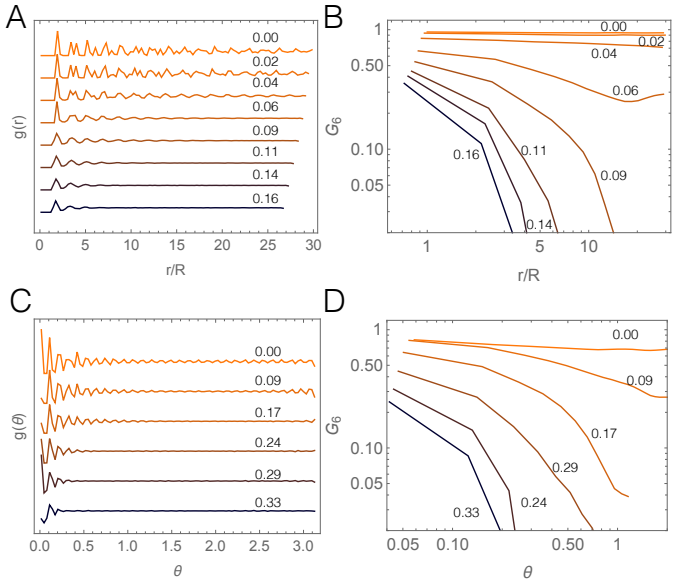

Fig. 2 Structural signatures of packings on flat surfaces and spherical surfaces reveal the transition from crystalline to amorphous phase with increasing anisotropy.(A) Pair correlation function $g(r)$ and (B) bond orientational correlation function $G_6(r)$ for bidispersed packings on flat surfaces. (C) Pair correlation function $g(\theta)$ and (D) bond orientational correlation function $G_6(\theta)$ for ellipsoidal packings of different anisotropy on spherical surfaces. Numbers indicate the value of anisotropy.

$$R^2 = \frac{1}{2}\sum_{i\neq j}\frac{d_{ij}}{n^2} \quad (1)$$

where d_{ij} is the distance between pairs of sites (i, j) and n is the number of sites, scales with the number of sites like $n \propto R^D$ where D is the fractal dimension. In two dimensions this has a value at p_c of $91/48 = 1.896$ independent of the structure of the system[37,57–61]. Many disordered systems, both discrete[58,59,62] and continuous[57,63–67] lie in this class, including forest fires, distribution of oil inside porous rock, the diffusion of atoms and conductivity of electrical networks[36,37].

An important feature of the packing problems considered is that they involve a finite number of particles, either for reasons of tractability or because they occur in compact geometries. In finite systems, the percolation transition becomes second order. For example, the fraction of simulations $u(p)$ that yield a globally connected cluster as a function of p is, in an infinite system, the unit step function $\theta(p - p_c)$ centered on the percolation point p_c. At finite N, $u(p)$ become sigmoidal in shape and converges toward $\theta(p - p_c)$ as the number of particles is increased. The value of p_c may therefore be extrapolated from a sequence of simulations of different size[58,59,66,68]. An alternative approach is to study the cluster size R as a function of p, which saturates at $p_R(N)$ as R approaches the system size[35]. The saturation point converges on p_c as $N \to \infty$. These different definitions need not necessarily coincide in finite systems.

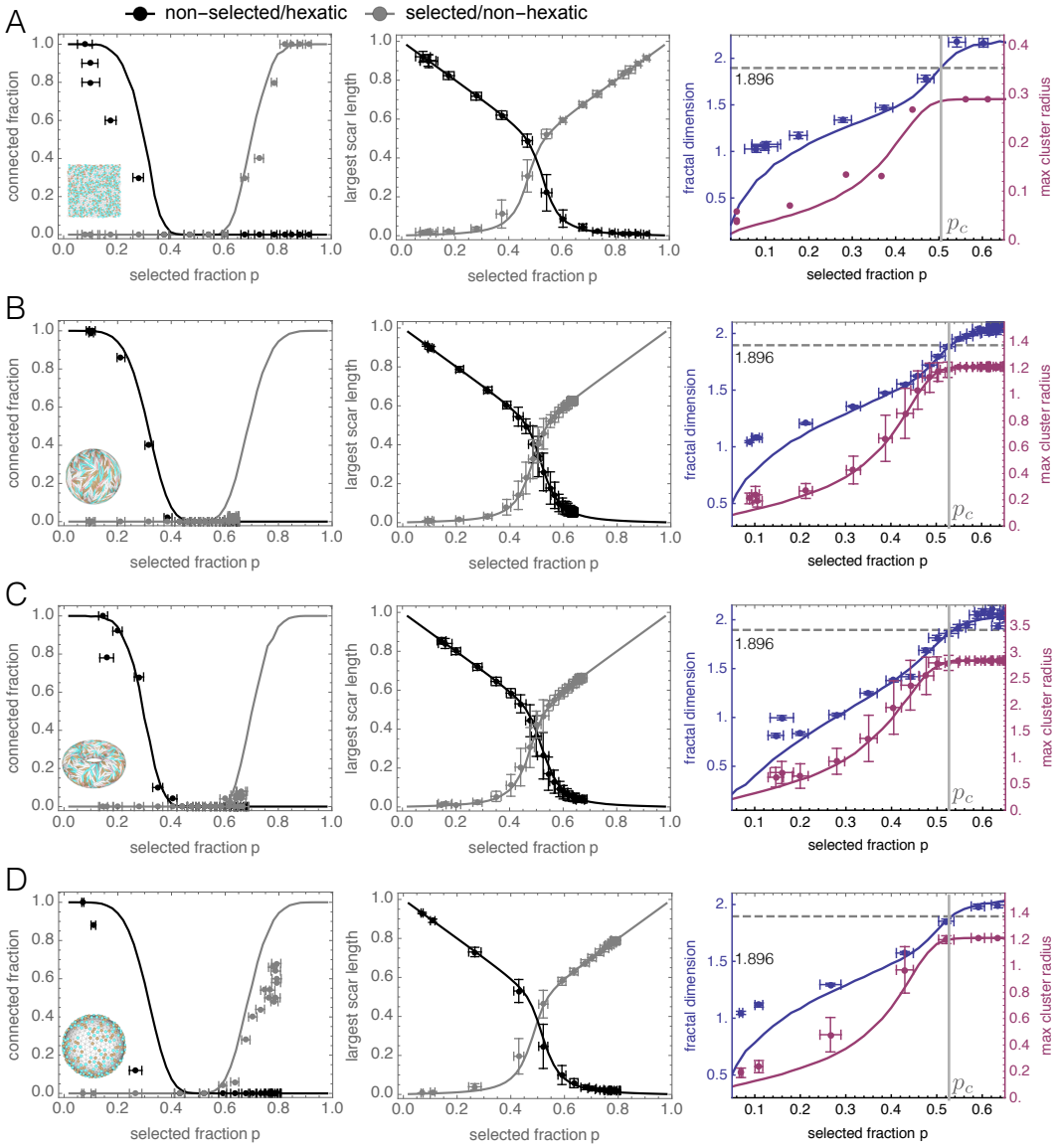

Fig. 3 Size and structure of defect networks is well predicted by a percolation model for several different anisotropy scenarios. (A) For bidispersed packings on flat surfaces, fraction of packings with connected spanning structure(left), fraction of particles in the largest connected component(middle), cluster radius of the largest connected component and fractal dimensions(right) as a function of defect fraction p. Data points are calculated from an ensemble of packings as described in the text; solid lines are the predictions of a percolation model with no fitting parameters. (B)—(D) show corresponding figures for ellipsoid packings on sphere, ellipsoid packings on torus and generalized Thomson problem. Error bars indicate standard deviation computed from our dataset.

Further, in contrast to the canonical site and bond percolation problems described above where p is a parameter that can be directly varied—in these problems p is the fraction of sites or bonds chosen on a specified lattice—here in packing problems it is the degree of anisotropy that is varied. The neighbor graphs and defect subgraphs are not known ahead of time and must be determined from the packing. We therefore identify p as the fraction of sites that lie in the defect subgraphs. This identification enables us to make an explicit comparison between a system that is not manifestly in the percolation universality class with one that is by construction: In each of scenarios considered, we create a zero anisotropy packing—which is of course crystalline—and compute its neighbor graph. We then study the site percolation problem on this graph, where we randomly select p fraction of sites iteratively and investigate their structure for every trial.

We may now examine the growth and structure of the clusters in the percolation model. The fraction of trials where the selected sites connect into a spanning structure is counted and showed as gray lines in left column of Fig. 3. The fraction becomes nonzero at around $p_c = 0.5$ on flat surfaces and $p_c = 0.55$ on spherical or toroidal surfaces, which is in good agreement with previous literature[35,58,59].We also compute the fraction of sites in the largest connected component, displayed as gray lines in the middle column of Fig. 3. In addition the structures of unselected sites are also computed and the corresponding results are displayed as black lines, which has the mirror symmetry compared with those of the selected sites as expected. The largest cluster radius R and fractal dimension of the selected sites are shown as a function of p in right column of Fig. 3. The radius saturates at the percolation transition p_c mentioned above where the value of fractal dimension is consistent with the universal value of 1.896, marked by the dash lines.

We further compare the structure of the defect subgraphs with this percolation model where the non-hexatic defects are recognized as the selected sites and the hexatic particles are treated as unselected sites. We compute the fraction of packings whose defects form a globally spanning structure, the fraction of sites in the largest defect subgraphs, the largest radius of the defect subgraphs and fractal dimension. The corresponding quantities are overlaid onto the curves of percolation model as dots in Fig. 3, described quite well by the model with no fitting parameters. The deviation of those dots from the curves is likely due to the finite-size effect. To plot those curves from the percolation model, we selected fraction p of particles thousands of times on the same lattice. However we can only generate a finite number of packings. Another possible reason is the existence of rattlers[46], i.e. particles that don't contribute to the connected networks. Therefore these rattlers can slightly reduce the fraction of packings that have a system-spanning structure. Nonetheless the agreement, particularly around the percolation point, is very good indeed, showing that the growth and structure of the clusters are well predicted by percolation theory. Note that for ellipsoid packings showed in Fig. 3B and C, the fraction of defects, represented by selected fraction, just exceeds the percolation threshold since the defect ratios saturate at around that value, as showed in Fig. 1C.

3 Conclusions

In this work, we have considered the emergence, elongation and global connection of defect structures as a function of different kinds of anisotropy. Besides bidispersity on flat and curved surfaces that link our work to the well-explored KTHNY transition, we demonstrate that elongating particles, or changing the nature of the interaction have a similar effect: anisotropy induces dislocations that cause the system to successively lose translational and orientational order, during which process the newly generated dislocations gradually form a globally connected cluster. We have further shown that structural features of the clusters, e.g. fractal dimension, are well predicted by the percolation model.

Our results suggest an apparent universality in that the defect structures that emerge when adding anisotropy to a crystalline system appear to be independent of the source of anisotropy. Bidispersity on the flat surface or on the surface of a sphere yield similar results to elongating particles or soft long-range interactions, or to packings on the surface of a torus. Intriguingly, our results for ellipsoidal particles show that the defect fraction only just exceeds the percolation threshold: we speculate that there may exist kinds of anisotropy that do not yield percolating defects and hence suppress the amorphous phase. One possible strategy to do so is to consider mixtures of particles that together form a tessellating structure; e.g. octagons and suitably sized squares, girih tiles[69]. Continuously deforming from uniform spheres towards such special configurations might eliminate the percolation effect. We suspect that other strategies might exist, perhaps involving non-convex particles for example as recent paper shows they can change the geometrical percolation threshold[70], and this newfound connection between particle shape and defect structure should open new avenues for tunability in the mechanics of particulate media.

4 Methods

Packing algorithm for ellipsoidal particles

Our algorithm to pack spherical particles is as described above and in previous work[35,47,48]. The extension to ellipsoidal particles involves modifications to overlap detection and diffusion as follows: The range parameter σ_{ij} is given by,

$$\sigma_{ij} = 2b/\sqrt{1-\frac{\chi}{2}\left(\frac{\hat{d_{ij}}\cdot\hat{u_i}+\hat{d_{ij}}\cdot\hat{u_j}}{1+\chi(\hat{u_i}\cdot\hat{u_j})}+\frac{\hat{d_{ij}}\cdot\hat{u_i}-\hat{d_{ij}}\cdot\hat{u_j}}{1-\chi(\hat{u_i}\cdot\hat{u_j})}\right)},$$

where a and b are the half lengths of the major and minor axes, $\chi = (a^2-b^2)/(a^2+b^2)$, $\hat{u}$ is a unit vector describing the overall orientation of the particle and $\hat{d_{ij}}$ is the unit vector pointing from one center to the other. If the center-to-center distance d_{ij} is smaller than the range parameter σ_{ij}, there is overlap. This criterion has been successfully implemented in other work[71–74]. If two ellipsoidal particles overlap, we exert the Gaussian model potential[75]

$$V(u_i,u_j,d_{ij}) = \varepsilon_0\left[1-\chi^2(\hat{u_i}\cdot\hat{u_j})^2\right]^{-1/2}\exp\left(-d_{ij}^2/\sigma_{ij}^2\right),$$

where ε_0 is the strength parameter, to remove the overlaps by gradient descent.

Diffusion of particles is another feature of our algorithm.

Spheres can diffuse simply by Langevin equation

$$\mathbf{x}_i^{'}(t+\delta t) = \mathbf{x}_i(t) + \eta_i\sqrt{2D\delta t},$$

where η_i is a random step drawn from Gaussian distribution, D is the diffusion constant such that $\sqrt{2D\delta t}$ determines the variance of the displacement for a timestep δt. For ellipsoids, we must also account for rotations. First we rotate the director of an ellipsoid by

$$\delta\theta(\delta t) = \eta_\theta\sqrt{2D_\theta\delta t}.$$

Then in the local coordination system $\tilde{x}$ and $\tilde{y}$ along the major and minor axes, it is displaced by

$$\delta r(\delta t) = \eta_a\sqrt{2D_a\delta t}\tilde{x} + \eta_b\sqrt{2D_b\delta t}\tilde{y}.$$

Finally we transform this local displacement into the global coordinate system by multiplying the rotation matrix[76].

Orientational correlation on spherical surfaces

Here we describe how to find the icosahedron that align with the defects following the method previously reported[29]. A non-trivial icosahedrally symmetric function can be defined as

$$h_6(\hat{x}) = Y_{6,0}(\hat{x}) + \sqrt{7/11}(Y_{6,-5}(\hat{x}) - Y_{6,5}(\hat{x})),$$

where Y is the spherical harmonics. The positions of local max values align with the vertices of an icosahedron. The defects on the spherical surface can be rotated by the rotational matrix

$$R_\omega(\theta,\phi) = \begin{pmatrix} \cos\theta & 0 & \sin\theta \\ 0 & 1 & 0 \\ -\sin\theta & 0 & \theta \end{pmatrix}\begin{pmatrix} \cos\phi & -\sin\phi & 0 \\ \sin\phi & \cos\phi & 0 \\ 0 & 0 & 1 \end{pmatrix}.$$

Then (θ,ϕ) is computed by minimizing $\sum_i h_6(R_\omega(\theta,\phi)\cdot\overrightarrow{r_i})$ where $\overrightarrow{r_i}$ represents coordinates of defects. The inverse rotation gives the icosahedron that align with the defects.

Conflicts of interest

There are no conflicts to declare.

Acknowledgments

This material is based upon work supported by the National Science Foundation under Grant No. DMR-1654283. One of the authors (TJA) thanks the Kavli Institute for Theoretical Physics ACTIVE'20 program which was supported in part by NSF Grant No. PHY-1748958, NIH Grant No. R25GM067110, and the Gordon and Betty Moore Foundation Grant No. 2919.02

Notes and references

1 M. J. Bowick and L. Giomi, *Advances in Physics*, 2009, **58**, 449–563.
2 S. Torquato and F. H. Stillinger, *Reviews of Modern Physics*, 2010, **82**, 2633.
3 A. Baule and H. A. Makse, *Soft Matter*, 2014, **10**, 4423–4429.
4 V. N. Manoharan, *Science*, 2015, **349**, year.
5 B. Li, D. Zhou and Y. Han, *Nature Reviews Materials*, 2016, **1**, 1–13.
6 S. Torquato, *The Journal of Chemical Physics*, 2018, **149**, 020901.
7 D. R. Nelson, M. Rubinstein and F. Spaepen, *Philosophical Magazine A*, 1982, **46**, 105–126.
8 M. Rubinstein and D. R. Nelson, *Physical Review B*, 1982, **26**, 6254.
9 A. Bausch, M. Bowick, A. Cacciuto, A. Dinsmore, M. Hsu, D. Nelson, M. Nikolaides, A. Travesset and D. Weitz, *Science*, 2003, **299**, 1716–1718.
10 M. J. Bowick, D. R. Nelson and A. Travesset, *Physical Review B*, 2000, **62**, 8738.
11 W. T. Irvine, V. Vitelli and P. M. Chaikin, *Nature*, 2010, **468**, 947–951.
12 F. L. Jiménez, N. Stoop, R. Lagrange, J. Dunkel and P. M. Reis, *Physical Review Letters*, 2016, **116**, 104301.
13 S. Williams and A. Philipse, *Physical Review E*, 2003, **67**, 051301.
14 A. Donev, I. Cisse, D. Sachs, E. A. Variano, F. H. Stillinger, R. Connelly, S. Torquato and P. M. Chaikin, *Science*, 2004, **303**, 990–993.
15 P. Chaikin, A. Donev, W. Man, F. H. Stillinger and S. Torquato, *Industrial & Engineering Chemistry Research*, 2006, **45**, 6960–6965.
16 Z. Yao and M. O. De La Cruz, *Proceedings of the National Academy of Sciences*, 2014, **111**, 5094–5099.
17 D. R. Nelson, *Defects and geometry in condensed matter physics*, Cambridge University Press, 2002.
18 B. Halperin and D. R. Nelson, *Physical Review Letters*, 1978, **41**, 121.
19 D. R. Nelson and B. Halperin, *Physical Review B*, 1979, **19**, 2457.
20 A. Young, *Physical Review B*, 1979, **19**, 1855.
21 E. P. Bernard and W. Krauth, *Physical Review Letters*, 2011, **107**, 155704.
22 W. Qi, A. P. Gantapara and M. Dijkstra, *Soft Matter*, 2014, **10**, 5449–5457.
23 J. A. Anderson, J. Antonaglia, J. A. Millan, M. Engel and S. C. Glotzer, *Physical Review X*, 2017, **7**, 021001.
24 S. C. Kapfer and W. Krauth, *Physical Review Letters*, 2015, **114**, 035702.
25 A. Hajibabaei and K. S. Kim, *Physical Review E*, 2019, **99**, 022145.
26 P. Digregorio, D. Levis, A. Suma, L. F. Cugliandolo, G. Gonnella and I. Pagonabarraga, *Physical Review Letters*, 2018, **121**, 098003.
27 S. Paliwal and M. Dijkstra, *Physical Review Research*, 2020, **2**, 012013.
28 S. P. Giarritta, M. Ferrario and P. Giaquinta, *Physica A: Statistical Mechanics and its Applications*, 1992, **187**, 456–474.
29 R. E. Guerra, C. P. Kelleher, A. D. Hollingsworth and P. M. Chaikin, *Nature*, 2018, **554**, 346–350.
30 J.-P. Vest, G. Tarjus and P. Viot, *The Journal of Chemical Physics*, 2018, **148**, 164501.
31 H. Seung and D. R. Nelson, *Physical Review A*, 1988, **38**, 1005.

32 V. Vitelli, J. B. Lucks and D. R. Nelson, *Proceedings of the National Academy of Sciences*, 2006, **103**, 12323–12328.

33 L. Giomi and M. Bowick, *Physical Review B*, 2007, **76**, 054106.

34 L. Giomi and M. J. Bowick, *Physical Review E*, 2008, **78**, 010601.

35 A. M. Mascioli, C. J. Burke, M. Q. Giso and T. J. Atherton, *Soft Matter*, 2017, **13**, 7090–7097.

36 G. Grimmett, *Percolation*, Springer, 1999.

37 D. Stauffer and A. Aharony, *Introduction to percolation theory*, Taylor & Francis, 2018.

38 A. Dinsmore, M. F. Hsu, M. Nikolaides, M. Marquez, A. Bausch and D. Weitz, *Science*, 2002, **298**, 1006–1009.

39 J. Hou, M. Li and Y. Song, *Angewandte Chemie International Edition*, 2018, **57**, 2544–2553.

40 S. Sacanna and D. J. Pine, *Current Opinion in Colloid & Interface Science*, 2011, **16**, 96–105.

41 S. Grosser, J. Lippoldt, L. Oswald, M. Merkel, D. M. Sussman, F. Renner, P. Gottheil, E. W. Morawetz, T. Fuhs, X. Xie *et al.*, *Physical Review X*, 2021, **11**, 011033.

42 A. Pérez-Garrido, M. Dodgson and M. Moore, *Physical Review B*, 1997, **56**, 3640.

43 M. Bowick, A. Cacciuto, D. R. Nelson and A. Travesset, *Physical Review Letters*, 2002, **89**, 185502.

44 D. J. Wales and S. Ulker, *Physical Review B*, 2006, **74**, 212101.

45 B. D. Lubachevsky and F. H. Stillinger, *Journal of Statistical Physics*, 1990, **60**, 561–583.

46 A. Donev, S. Torquato, F. H. Stillinger and R. Connelly, *Journal of Applied Physics*, 2004, **95**, 989–999.

47 C. J. Burke, B. L. Mbanga, Z. Wei, P. T. Spicer and T. J. Atherton, *Soft Matter*, 2015, **11**, 5872–5882.

48 Z. Xie, C. J. Burke, B. Mbanga, P. T. Spicer and T. J. Atherton, *Soft Matter*, 2019, **15**, 9587–9596.

49 V. Luchnikov, N. Medvedev, L. Oger and J.-P. Troadec, *Physical Review E*, 1999, **59**, 7205.

50 F. M. Schaller, S. C. Kapfer, M. E. Evans, M. J. Hoffmann, T. Aste, M. Saadatfar, K. Mecke, G. W. Delaney and G. E. Schröder-Turk, *Philosophical Magazine*, 2013, **93**, 3993–4017.

51 T. M. Truskett, S. Torquato, S. Sastry, P. G. Debenedetti and F. H. Stillinger, *Physical Review E*, 1998, **58**, 3083.

52 A. Donev, S. Torquato and F. H. Stillinger, *Physical Review E*, 2005, **71**, 011105.

53 K. Bagchi, H. C. Andersen and W. Swope, *Physical Review Letters*, 1996, **76**, 255.

54 D. Li and S. A. Rice, *Physical Review E*, 2005, **72**, 041506.

55 Y. Han, N. Ha, A. Alsayed and A. Yodh, *Physical Review E*, 2008, **77**, 041406.

56 S. Prestipino, F. Saija and P. V. Giaquinta, *Physical Review Letters*, 2011, **106**, 235701.

57 B. Lorenz, I. Orgzall and H.-O. Heuer, *Journal of Physics A: Mathematical and General*, 1993, **26**, 4711.

58 D. He, N. Ekere and L. Cai, *Physical Review E*, 2002, **65**, 061304.

59 Y. Han, J. Lee, S. Q. Choi, M. C. Choi and M. W. Kim, *EPL (Europhysics Letters)*, 2015, **109**, 66002.

60 J. Zierenberg, N. Fricke, M. Marenz, F. Spitzner, V. Blavatska and W. Janke, *Physical Review E*, 2017, **96**, 062125.

61 S. Mitra, D. Saha and A. Sensharma, *Physical Review E*, 2019, **99**, 012117.

62 N. Lebovka, M. Lisunova, Y. P. Mamunya and N. Vygornitskii, *Journal of Physics D: Applied Physics*, 2006, **39**, 2264.

63 S. B. Lee and S. Torquato, *Physical Review A*, 1990, **41**, 5338.

64 J. Quintanilla, S. Torquato and R. M. Ziff, *Journal of Physics A: Mathematical and General*, 2000, **33**, L399.

65 J. A. Quintanilla and R. M. Ziff, *Physical Review E*, 2007, **76**, 051115.

66 Y.-B. Yi and A. Sastry, *Physical Review E*, 2002, **66**, 066130.

67 J. Asikainen and T. Ala-Nissila, *Physical Review E*, 2000, **61**, 5002.

68 M. Newman and R. M. Ziff, *Physical Review Letters*, 2000, **85**, 4104.

69 P. J. Lu and P. J. Steinhardt, *Science*, 1106–1110, **315**, year.

70 J. Lin, H. Chen and W. Xu, *Physical Review E*, 2018, **98**, 012134.

71 P. Padilla and E. Velasco, *The Journal of Chemical Physics*, 1997, **106**, 10299–10310.

72 C. Anquetil-Deck, D. J. Cleaver and T. J. Atherton, *Physical Review E*, 2012, **86**, 041707.

73 Z. Zeravcic, N. Xu, A. Liu, S. Nagel and W. van Saarloos, *EPL (Europhysics Letters)*, 2009, **87**, 26001.

74 A. DeBenedictis, T. J. Atherton, C. Anquetil-Deck, D. J. Cleaver, D. B. Emerson, M. Wolak and J. H. Adler, *Physical Review E*, 2015, **92**, 042501.

75 B. J. Berne and P. Pechukas, *The Journal of Chemical Physics*, 1972, **56**, 4213–4216.

76 Y. Han, A. M. Alsayed, M. Nobili, J. Zhang, T. C. Lubensky and A. G. Yodh, *Science*, 2006, **314**, 626–630.